Computed radial stresses in a concrete target penetrated by a steel projectile

G.R. Johnson[a], S.R. Beissel[a], T.J. Holmquist[a] & D.J. Frew[b]

[a] *Alliant Techsystems, Incorporated, Hopkins, Minnesota, USA*

[b] *U.S. Army Waterways Experiment Station, Vicksburg, Mississippi, USA*

EMail: gordon_johnson@atk.com

Abstract

This paper provides computed radial stresses and penetration depth for a concrete target that is impacted by an ogive-nose steel projectile at a velocity of 315 m/s. The computed results are in good agreement with recently published experimental results. Also included is a description of the concrete model.

1 Introduction

The response of a steel projectile impacting concrete, rock and earth targets has been of interest for many years. The depth of penetration, the trajectory, the response of the projectile and the response of the target are all items of interest. A 2D axisymmetric computation of a steel projectile into earth media was presented by Thigpen[1] in 1974. A variety of 2D and 3D computational approaches was provided by Johnson, Stryk and Nixon[2] in 1988, and by Schwer and Day[3] in 1991. More recently, a 3D parametric computational study was performed by Johnson et. al.,[4] and a computational concrete material model was developed by Holmquist, Johnson and Cook.[5] This work focuses on the response of the concrete target, and the computed results are compared to the recent experimental results of Gran and Frew.[6] The computations are based on an explicit finite element algorithm,[7] an automatic sliding interface algorithm[8] and the HJC concrete constitutive model.[5]

2 Concrete Model

A general overview of the HJC concrete model is presented in Figure 1. The normalized equivalent stress is defined as $\sigma* = \sigma / f_c'$, where σ is the actual equivalent stress and f_c' is the quasi-static uniaxial compressive strength. The specific expression is

$$\sigma* = [A(1 - D) + BP*^N][1 + C \ln \dot{\varepsilon}*] \tag{1}$$

where D is the damage $(0 \leq D \leq 1.0)$, $P* = P / f_c'$ is the normalized pressure (where P is the actual pressure), and $\dot{\varepsilon}* = \dot{\varepsilon} / \dot{\varepsilon}_o$ is the dimensionless strain rate (where $\dot{\varepsilon}$ is the actual strain rate and $\dot{\varepsilon}_o = 1.0 \text{ s}^{-1}$ is the reference strain rate).   The normalized maximum tensile hydrostatic pressure is $T* = T / f_c'$, where T is the maximum tensile hydrostatic pressure the material can withstand.

The material constants are A, B, N, C and $\sigma*_{max}$, where A is the $\sigma*'$ intercept at $P* = 0$ and $\dot{\varepsilon}* = 1.0$, B is the normalized pressure hardening coefficient, N is the pressure hardening exponent, C is the strain rate coefficient, and $\sigma*_{max}$ is the normalized maximum strength that can be developed.

The damage for fracture is accumulated from both equivalent plastic strain and plastic volumetric strain, and is expressed as

$$D = \sum \frac{\Delta \varepsilon_p + \Delta \mu_p}{\varepsilon_p^f + \mu_p^f} \tag{2}$$

where $\Delta \varepsilon_p$ and $\Delta \mu_p$ are the increments in equivalent plastic strain and plastic volumetric strain, respectively, during a cycle of integration; and $\varepsilon_p^f + \mu_p^f = f(P)$ is the plastic strain to fracture under a constant pressure, P. The specific expression is

$$\varepsilon_p^f + \mu_p^f = D_1(P* + T*)^{D_2} \tag{3}$$

where D_1 and D_2 are constants and P* and T* are as defined previously. As is evident from eqn (3), the concrete material cannot undergo any plastic strain at $P* = -T*$ without fracturing, and alternatively,
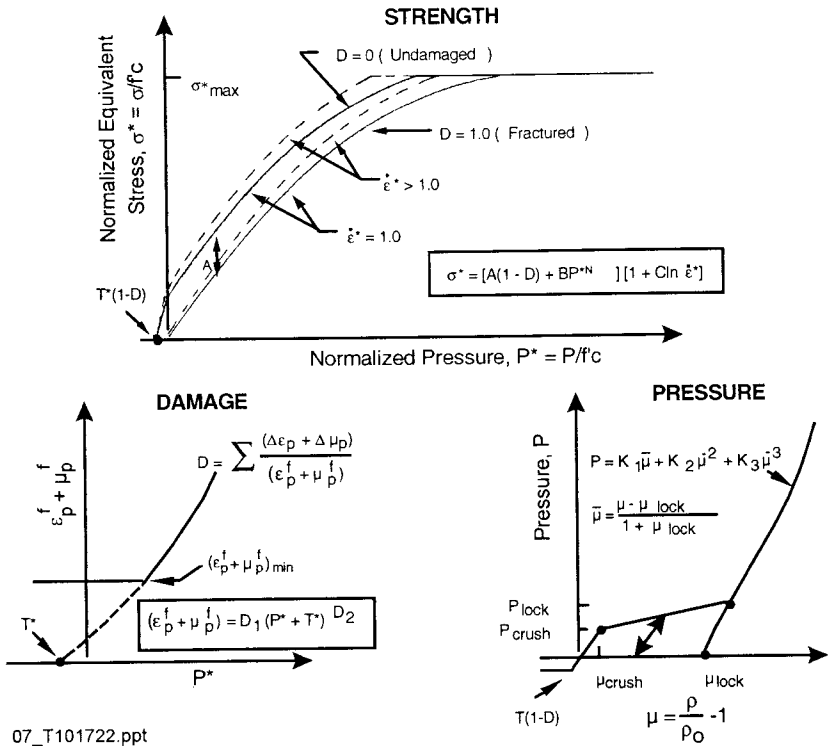
Figure 1. Description of the Concrete Model

the plastic strain to fracture increases as $P*$ increases. A third damage constant, $(\varepsilon_p^f + \mu_p^f)_{min}$, is provided to allow for a finite amount of plastic strain to fracture the material. This is included to suppress fracture from low magnitude tensile waves.

The first hydrostatic pressure-volume region is linear elastic and occurs at $P \leq P_{crush}$, where P_{crush} and μ_{crush} are the pressure and volumetric strain that occur in a uniaxial stress compression test, and T is as previously defined. The elastic bulk modulus is $K_{elastic} = P_{crush}/\mu_{crush}$.

The second region is the transition region and occurs at $P_{crush} < P < P_{lock}$. In this region, the air voids are gradually compressed out of the concrete producing plastic volumetric strain. Unloading in this region occurs along a modified path that is interpolated from the adjacent regions.

796   Structures Under Shock and Impact

The third region defines the relationship for fully dense material (all air voids removed from the concrete). The air voids are completely removed from the material when the pressure reaches P_{lock} and the relationship is

$$P = K_1 \bar{\mu} + K_2 \bar{\mu}^2 + K_3 \bar{\mu}^3 \qquad (4)$$

where

$$\bar{\mu} = \frac{\mu - \mu_{lock}}{1 + \mu_{lock}} \qquad (5)$$

The modified volumetric strain, $\bar{\mu}$, is used so that the constants (K_1, K_2, and K_3) are equivalent to those used for the material with no voids. The standard volumetric strain for this model is $\mu = \rho / \rho_O - 1$ for current density ρ and initial density ρ_O. The locking volumetric strain is $\mu_{lock} = \rho_{grain} / \rho_O - 1$; where ρ_{grain} is the grain density, which is identical to the density of the material with no air voids.

For tensile pressure, $P = K_{elastic}\mu$ in the elastic region, $P = K_1\bar{\mu}$ in the fully dense region, and the pressures are interpolated in the transition region. The interpolation factor is $F = (\mu_{max} - \mu_{crush})/(\mu_{plock} - \mu_{crush})$ where μ_{max} is the maximum volumetric strain reached prior to unloading and μ_{plock} is the volumetric strain at P_{lock}. A similar method is used for compressive unloading except that the higher order terms ($K_2\bar{\mu}^2$ and $K_3\bar{\mu}^3$) are included. The tensile pressure is limited to $T(1-D)$. The shear modulus (G) is proportional to the current bulk modulus, which is identical to using a constant Poisson's ratio.

The constants used for the model are shown below.

$\rho_O = 2250$ Kg/m^3	$P_{crush} = 13.6$ MPa	$D_1 = 0.03$
$A = 0.75$	$\mu_{crush} = 0.00058$	$D_2 = 1.0$
$B = 1.65$	$K_1 = 17,400$ MPa	$\left(\varepsilon_p^f + \mu_o^f\right)_{min} = 0.01$
$N = 0.76$	$K_2 = 38,800$ MPa	
$C = 0.007$	$K_3 = 29,800$ MPa	
$f_c' = 43$ MPa	$P_{lock} = 1,050$ MPa	
$\sigma_{max}^* = 11.7$	$\mu_{lock} = 0.10$	
$G_O = 16,400$ MPa	$T = 2.4$ MPa	

Some of the procedures used to determine the constants are provided with the original description of the model.[5]   The constants were determined from a variety of experimental concrete data similar to the concrete used in the penetration tests.   Only the density (ρ_0) and the compressive strength (f_c') were adjusted to match the concrete used for the penetration tests.   All of the other constants were determined previously.

Figure 2 shows a comparison of concrete test data[6] with the model predictions. Here the pressure is given as a function of the compressive volumetric strain, $-\varepsilon_v$. This is a different definition than that used for the concrete model, with $\varepsilon_v = V / V_o - 1$ where V is the current volume and V_o is the initial volume. For small volumetric strains $\mu \approx -\varepsilon_v$. The test data were obtained under uniaxial strain conditions, and it can be seen that the model generally predicts higher pressures than the test data.

Figure 2 also shows a comparison of the compressive axial stresses. The net stress (tension positive) is $\sigma_z = s_z - P$ where s_z is the deviator stress (tension positive) and P is the hydrostatic pressure (compression positive) from the upper half of Figure 2.   Again, the model generally predicts higher stresses than the test data.

Figure 3 shows the equivalent stress, $\overline{\sigma}$, as a function of the pressure.   This relationship is taken from the data in Figure 2.   The equivalent stress is highly dependent on the pressure, as represented by the material model in Figure 1 and eqn (1). Even though the unloading paths do not coincide, the envelope predicted by the model is in good agreement with the test data.

Figure 4 shows another plot of pressure versus compressive volumetric strain. In Figure 2 the test conditions were uniaxial strain, but in Figure 4 the pressures were applied hydrostatically such that triaxial stress and strain conditions exist with no shear. Test data are shown for three tests with maximum hydrostatically applied pressures of $P_o = 50$, 150 and 300 MPa. Here the model underpredicts the pressures, whereas the model overpredicted the pressures for the uniaxial strain data of Figure 2. This is a general characteristic of concrete; it is stiffer under triaxial (hydrostatic) loading than under uniaxial strain loading.   This model represents an intermediate condition. In Figure 2 the model is too stiff for uniaxial strain loading and in Figure 4 it is too soft for triaxial (hydrostatic) loading.

798   Structures Under Shock and Impact
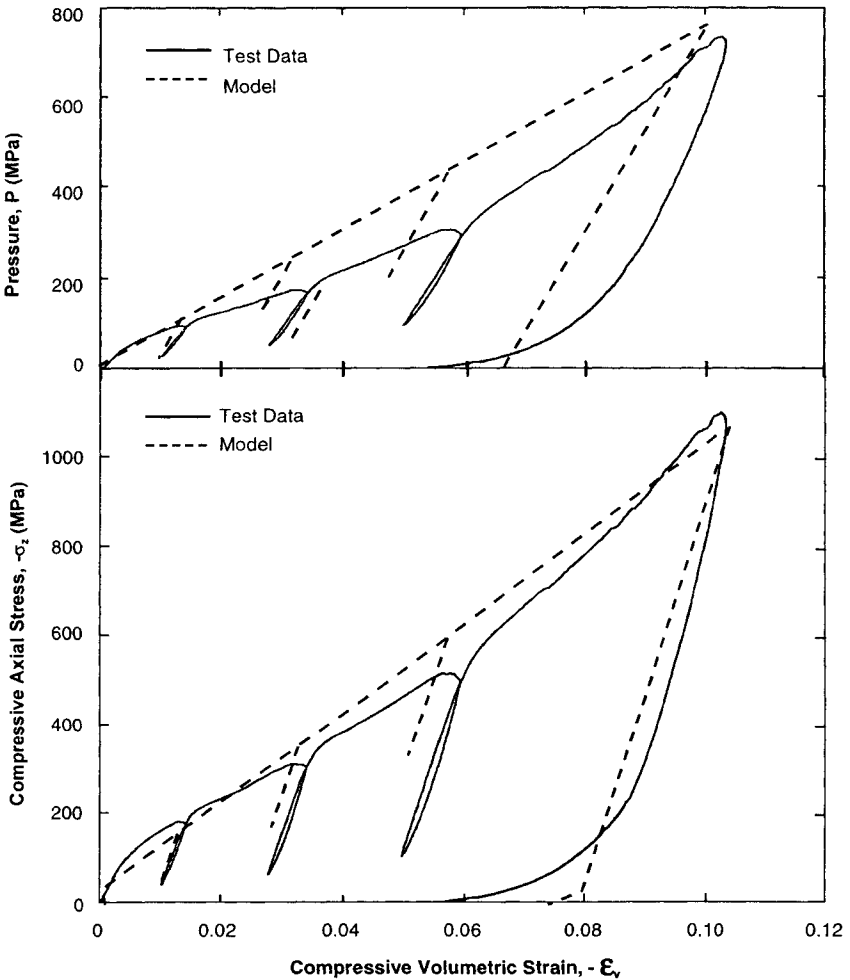
04_T101722.ppt

Figure 2.   Pressure and Compressive Axial Stress versus Compressive
Volumetric Strain for Uniaxial Strain Loading

Figure 5 shows equivalent stress versus compressive axial strain for
the three tests of Figure 4.   Here the initial conditions were specimens
that were hydrostatically loaded to pressures of $P_o = 50$, 150 and 300
MPa.   These specimens were then compressed in the axial direction
while maintaining the radial pressures.   Here, the model slightly
underpredicts the strength.   Nevertheless, the model appears to represent
all of the general characteristics of the concrete.

08_T101722.ppt
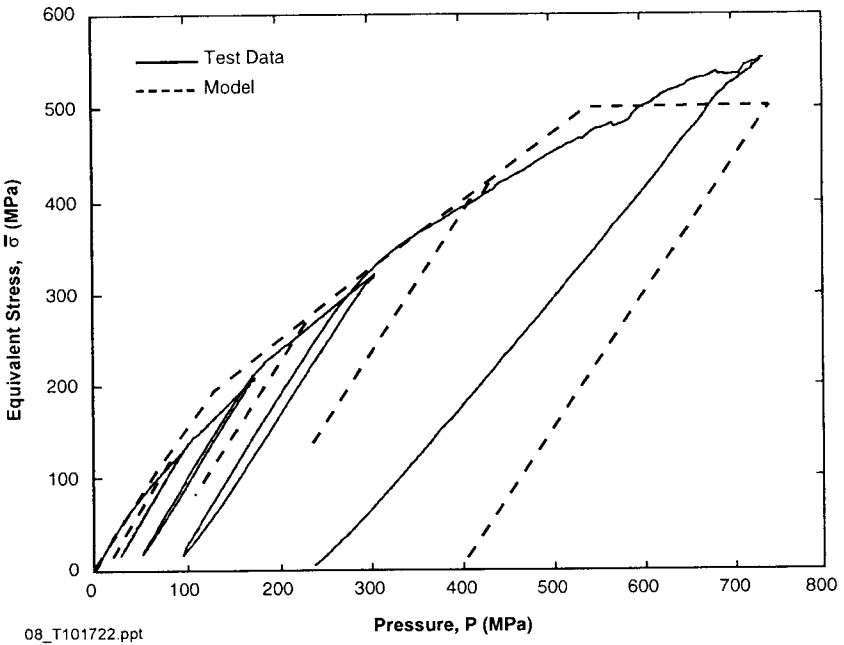
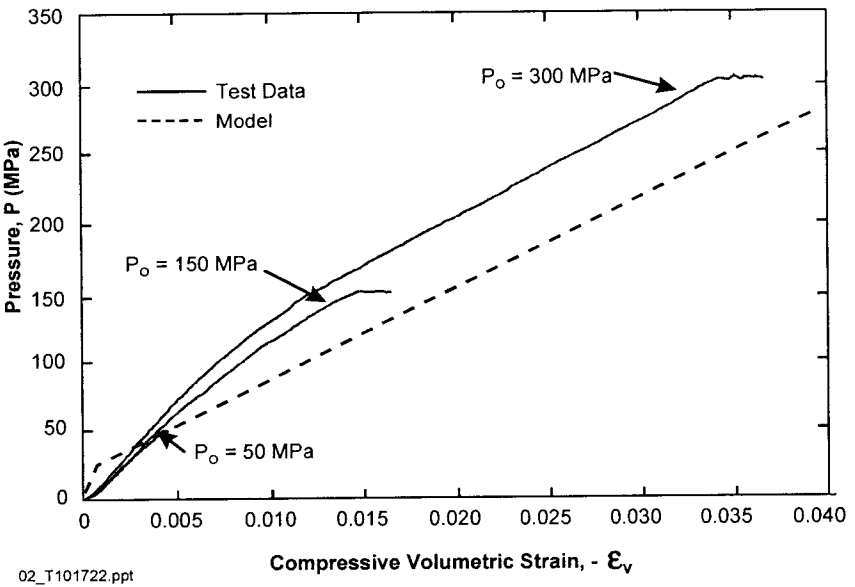Figure 3. Equivalent Stress versus Pressure for Uniaxial Strain Loading

02_T101722.ppt

Figure 4.   Pressure versus Compressive Volumetric Strain for Triaxial
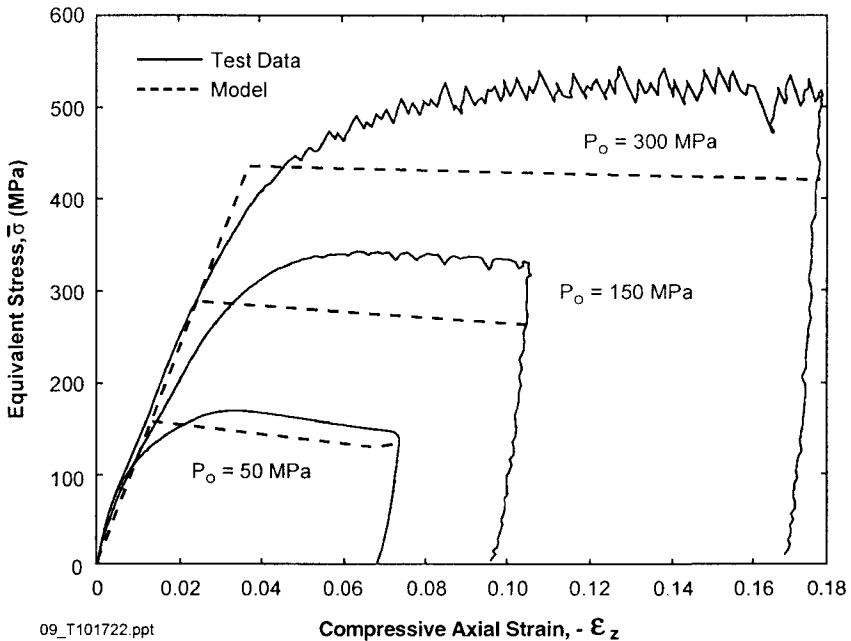(Hydrostatic) Loading

Figure 5. Equivalent Stress versus Compressive Axial Strain for Triaxial Loading

3 Computed Results

Figure 6 shows the configuration of the projectile and the target. Many of the dimensions are normalized by the radius of the projectile, $r_p = 25.4$ mm. Additional details concerning the geometry, the gages, and the location of the gages, are provided by Gran and Frew.[6] The steel projectile is essentially elastic, and the filler is represented by sand with the proper density.

The finite element grid contains 31,440 triangular elements for the projectile and the concrete target and 96 shell elements to represent the steel case around the target, for a total of 31,536 elements. An erosion strain of 3.0 was used.[8] For this class of problem, where there is no erosion in the projectile, computational erosion in this target is used simply to allow the integration time increment to remain larger. Also, friction was not included. This baseline problem required 9635 cycles of integration for $t_{max} = 150$ ms, and it required 2.78 hours of CPU time on an SGI R8000 computer.
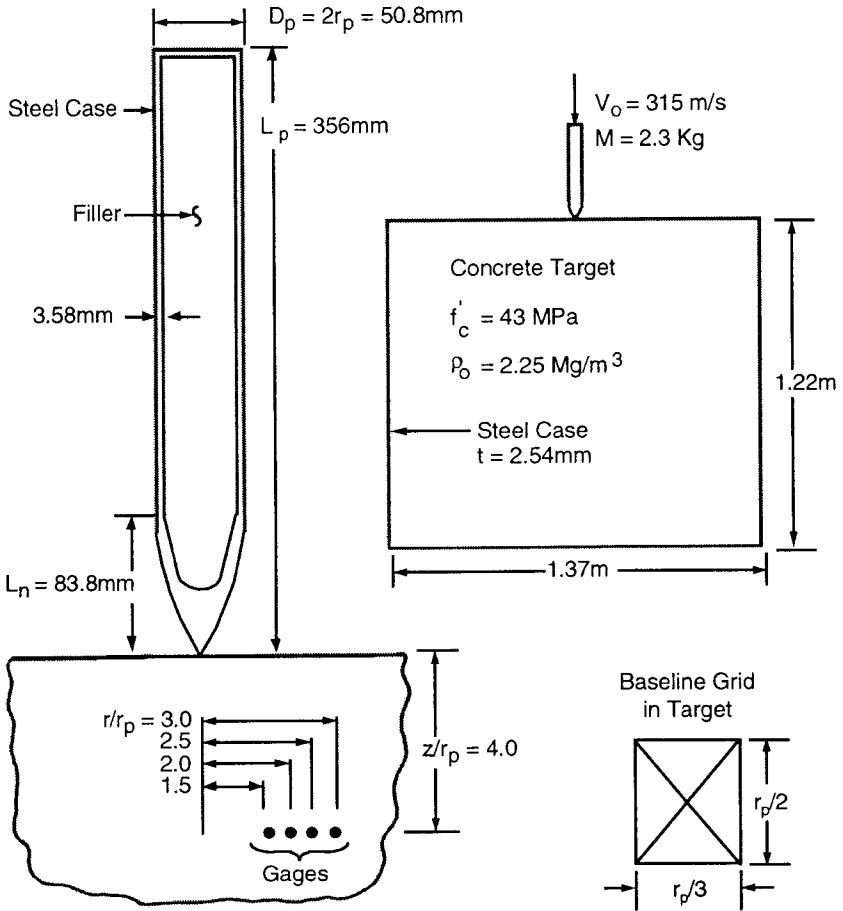
03_T101722.ppt

Figure 6. Description of the Problem

The erosion strain, grid size and friction parameters were varied independently to determine the sensitivity of the computed results. For the first case, the baseline problem was rerun with a higher erosion strain of 4.0. The maximum penetration was essentially unchanged, but 18,957 cycles of integration were required and the CPU time increased by a factor of 1.93 to 5.37 hours.

A very fine grid was also used. The nodal spacing was decreased by a factor of 2.0 such that there were 4.0 times more triangular elements in the target. For this problem, the maximum penetration increased by 4.0 percent, but the CPU time increased by a factor of 11.0 to 30.66 hours.

## 802   Structures Under Shock and Impact

The final parametric variation was to include a coefficient of sliding friction of 0.05 between the projectile and the concrete target. This resulted in the maximum penetration being decreased by 10.7 percent. Unfortunately, there are no experimental techniques available to adequately assess or predict frictional effects.

The finite element model, the concrete material model, and the other assumptions are all reasonable assumptions that would be made for production computations. The initial baseline computation was made with these assumptions, prior to having access to the experimental results. No attempt was made to modify the computations to provide better agreement with the experimental results.

Figure 7 shows a comparison of the experimental radial stresses[6] and the baseline computed radial stresses at normalized positions of r/r_p = 1.5, 2.0 and 2.5, and at z/r_p = 4.0. In all instances the computed results provide good general agreement with the experimental results. The computed arrival times and maximum stresses show excellent agreement, but the computed stresses drop off at later times than the test data stresses. Similarly, Figure 8 shows excellent agreement between the maximum radial stresses as a function of the radial positions of the gages. The test data in Figure 8 are for all gages at $z/r_p = 4.0$.

For $r/r_p = 1.5$ at the top of Figure 7, the sharp drop in the computed stress at 0.65 ms is due to the erosion strain of 3.0. (When an element erodes all of the stresses in that element are instantaneously set to zero.) This drop does not appear for an erosion strain of 4.0. However, the general response is similar for both erosion strains. Decreasing the erosion strain to 2.0 has a significant degrading effect on the stress responses. These effects are shown in Figure 9.

Figure 10 shows computed results. For a nominal impact velocity of 315 m/s, the baseline computed penetration is P = 0.161 m, or a normalized penetration of P/r_p = 6.34. Again, this falls within the range of the test data for the three tests, where the normalized penetration depths were 6.2, 6.9 and 7.3[6]. The lightly shaded regions in Figure 10 show partial damage (0.1 < D < 0.9) and the darkened regions represent high damage ($0.9 \leq D \leq 1.0$) in the concrete. Figure 10 also shows the responses for the high erosion strain computation and the fine grid computation. The penetration depths and damaged regions are very similar, but the crack patterns are different for the three computations.
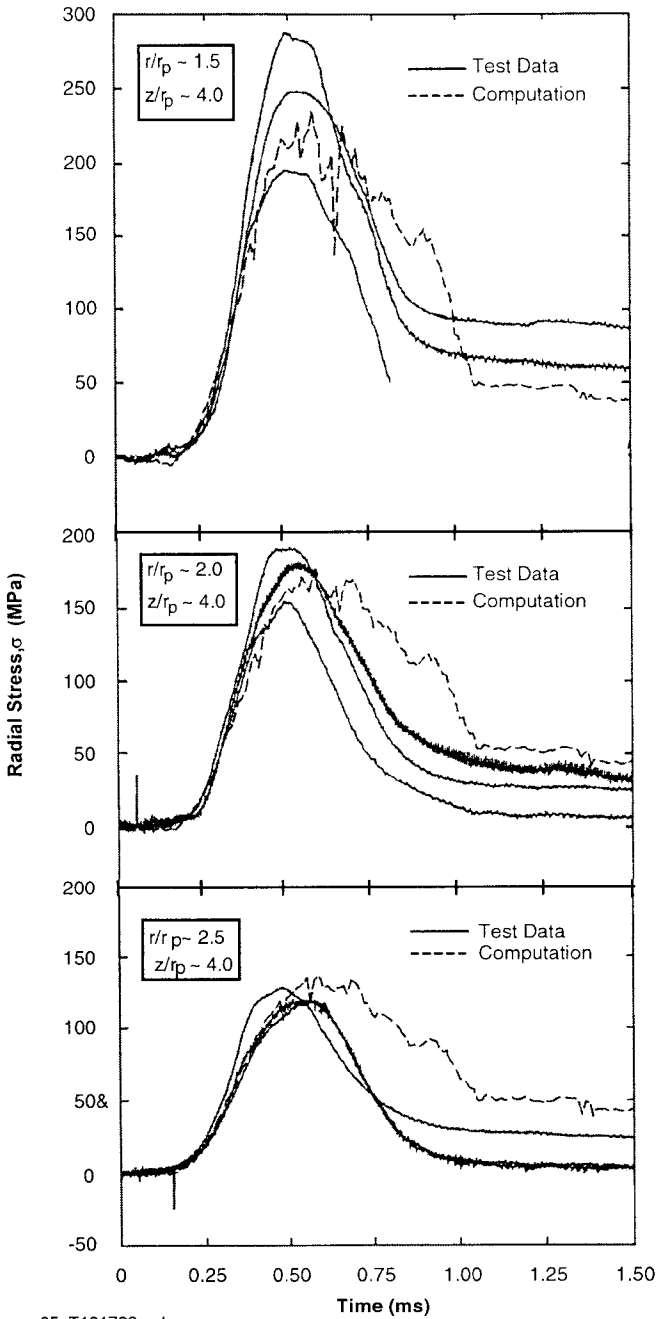
05_T101722.ppt

Figure 7.   Radial Stress versus Time at r/r_p = 1.5, 2.0 and 2.5, and at z/r_p = 4.0
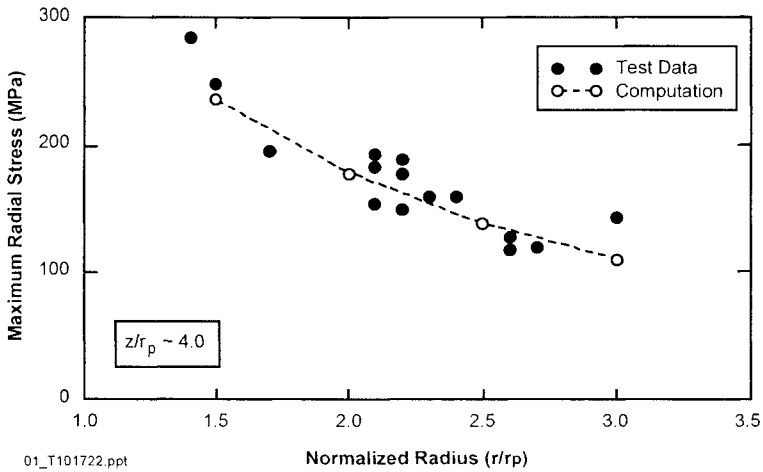
Figure 8. Maximum Radial Stress versus Normalized Radius
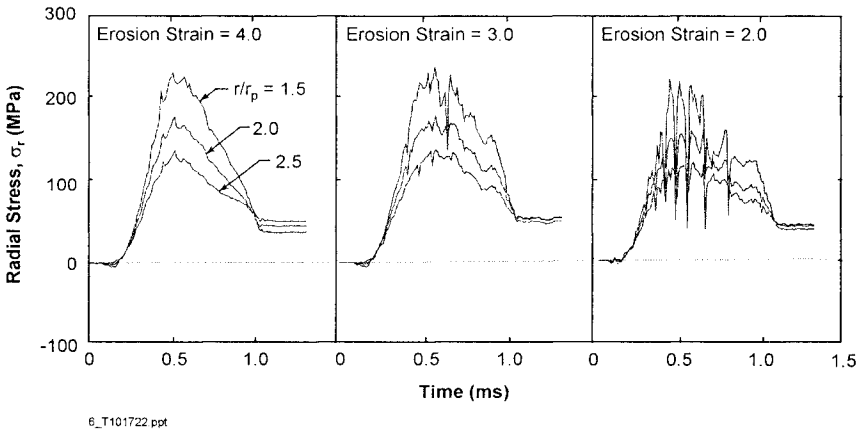

Figure 9. Radial Stress versus Time for Various Erosion Strains

5 Summary and Conclusions

Finite element penetration computations have been performed to compare computed results to recently published experimental results for radial stresses and depth of penetration in a concrete target. The concrete target was represented with the HJC concrete model. In all instances, the computed results provided good general agreement with the experimental results. The computed results also provide damage and crack patterns in the concrete.
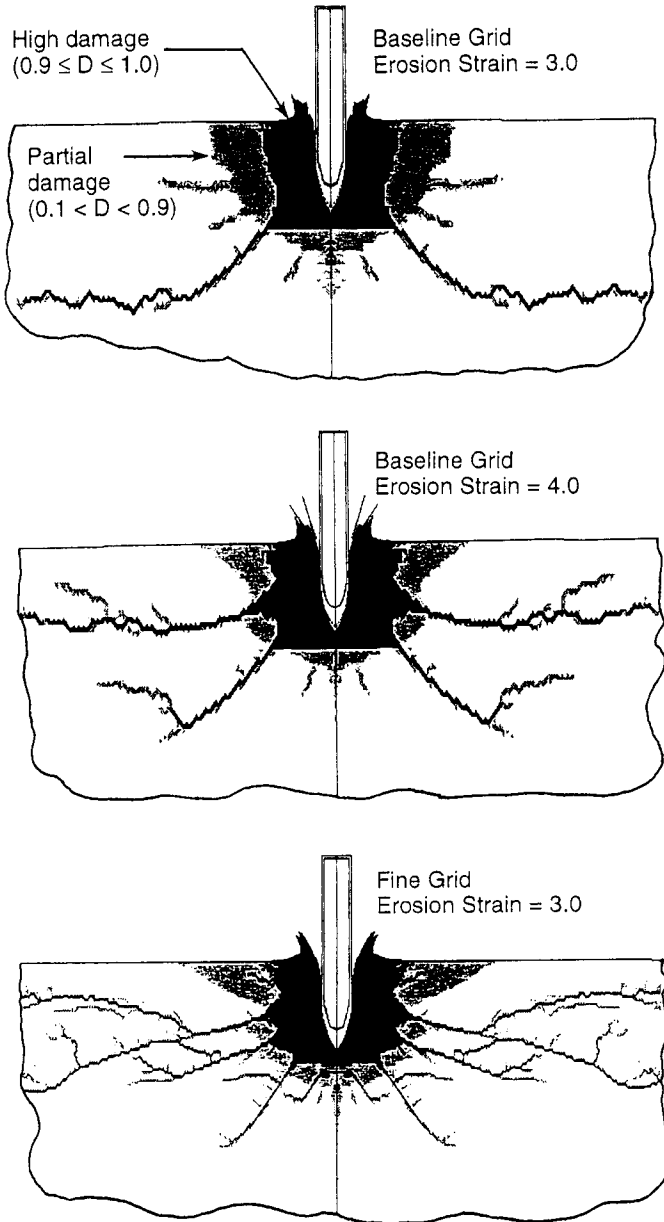
Figure 10.   Deformed Geometry and Damage Contours for the Baseline,
High Erosion Strain, and Fine Grid Computations at
t = 1.5 ms.

806   Structures Under Shock and Impact

Acknowledgment

References

[1] Thigpen, L., Projectile penetration of elastic-plastic earth media, *Journal of the Geotechnical Engineering Division, ASCE,* 1974.

[2] Johnson, G.R., Stryk, R.A., and Nixon, M.E., Two and three dimensional computational approaches for steel projectiles impacting concrete targets, *Impact: Effects of Fast Transient Loadings,* ed. W.J. Ammann, W.K. Liu, J.A. Studer and T. Zimmerman, 1988.

[3] Schwer, L.E. and Day, J., Computational techniques for penetration of concrete and steel targets by oblique impact of deformable projectiles, *Nuclear Engineering and Design, 125,* 1991.

[4] Johnson, G.R., Stryk, R.A., Schonhardt, J.A., Cook, W.H. and Collins, J.A., Effects of velocity, obliquity, and yaw for a penetrator impacting concrete targets, with and without reinforcing steel, *Proc. of Thirteenth International Symposium on Ballistics,* Stockholm, Sweden, 1992.

[5] Holmquist, T.J., Johnson, G.R., and Cook, W.H., A computational constitutive model for concrete subjected to large strains, high strain rates and high pressures, *Proc. of Fourteenth International Symposium on Ballistics,* Quebec City, Canada, 1993.

[6] Gran, J.K. and Frew, D.J., In-target stress measurements from penetration experiments into concrete by ogive-nose steel projectiles, *International Journal of Impact Engineering, 19,* 1997.

[7] Johnson, G.R., Dynamic response of axisymmetric solids to impact and spin, *AIAA Journal, 17,* 1979.

[8] Johnson, G.R., and Stryk, R.A., An automatic sliding interface algorithm for intense impulsive loading computations, *Communications in Numerical Methods in Engineering, 12,* 1996.